Tailoring olefin distribution via tuning rare earth metals in bifunctional Cu-RE/beta-zeolite catalysts for ethanol upgrading☆

Meijun Li [a],[*], Junyan Zhang [b], Stephen C. Purdy [a], Fan Lin [c], Kinga A. Unocic [d], Michael Cordon [a], Zili Wu [b],[d], Huamin Wang [c], Jacklyn Hall [e], A. Jeremy Kropf [e], Theodore R. Krause [e], Brian Davison [f], Zhenglong Li [a],[1], Andrew D. Sutton [a],[*]

[a] *Manufacturing Science Division, Oak Ridge National Laboratory, Oak Ridge, TN 37830, USA*
[b] *Chemical Sciences Division, Oak Ridge National Laboratory, Oak Ridge, TN 37830, USA*
[c] *Energy Processes & Materials Division and Institute for Integrated Catalysis, Pacific Northwest National Laboratory, Richland, WA 99354, USA*
[d] *Center for Nanophase Materials Sciences, Oak Ridge National Laboratory, Oak Ridge, TN 37830, USA*
[e] *Chemical Science and Engineering Division, Argonne National Laboratory, Lemont, IL 60439, USA*
[f] *Bioscience Division, Oak Ridge National Laboratory, Oak Ridge, TN 37830, USA*

ARTICLE INFO

ABSTRACT

Bioethanol to middle distillate technologies have offered a unique solution to produce renewable aviation fuel for decarbonizing the hard-to-electrify sectors. Here, we have developed the series of bimetallic Cu- and rare earth-containing (RE) Beta zeolite catalysts that yield high C_{3+} alkene selectivity from ethanol upgrading (>80% selectivity at ~100% conversion, 623 K). The formation rates of butene isomers to C_{5+} alkenes are linearly correlated with the strength of Lewis acidic RE identity, which follows the sequence of Yb_{12}/Beta >Y_7/Beta > Gd_{12}/Beta > Ce_{10}/Beta > La_{12}/Beta. Rate measurements indicate that the RE selection plays the vital role in altering the rate of the key competitive reactions within the ethanol-to-alkenes reaction network, namely C_4 alcohol dehydration and C-C chain growth, which dictate alkene product distributions. These findings indicate a feasible and promising method for tailoring alkene product distributions from ethanol upgrading, which is of notable significance to the generation of renewable middle distillates.

1. Introduction

The production of sustainable middle distillate fuels from renewable feedstocks is an important and promising strategy to decarbonize hard-to-electrify transportation sectors, such as aviation, marine and heavy-duty diesel applications. Due to its renewable nature and commercial availability, bio-derived ethanol has been recognized as one of the key C_2 platform chemicals for sustainable middle distillate fuels production [1–5]. Light olefins (C_{3+}), indispensable feedstocks for downstream oligomerization and hydrogenation to form of mid-range distillate hydrocarbons, can be efficiently synthesized from ethanol. Ethanol-to-olefins formation processes involve cascade reaction networks with either ethanol dehydration to ethylene or dehydrogenation to acetaldehyde prior to undergoing crucial carbon-carbon coupling steps [6–10].

Alcohol-to-jet fuel technologies have been performed commercially utilizing the reaction pathway of ethanol dehydration to ethylene followed by oligomerization to generate butene-rich olefin mixtures in either one- or two-step processes [11–13]. For the two-step process, the endothermic nature of ethanol dehydration necessitates a significant and continuous energy input which is compounded by the temperature differential between the dehydration and oligomerization units. In addition to having distinct reaction conditions, this two-step operation requires higher capital costs for multiple individual reactors. Although

coupling the two reaction steps together on one single catalyst can reduce both operational and capital costs, the current one-step process utilize Brønsted acidic zeolites that also catalyze significant side reactions which form aromatics and light paraffins due to the strong Brønsted acidity and confinement effects of the microporous environments [7,14,15]. Recent research efforts have focused on developing an alternative one-step process that reduces the energy consumption and mitigates undesirable side product formation [16–19]. This approach has focused on acetaldehyde as a key aldol condensation reactant for C_{3+} alkene formation and has been identifying catalysts that catalyze ethanol dehydrogenation to acetaldehyde and subsequent aldol condensation to form C_4 intermediates such as crotonaldehyde and butyraldehyde. The targeted reaction pathway requires multiple catalytic functionalities for (de)hydrogenation, aldol condensation, Meerwein-Ponndorf-Verley (MPV) reduction, and dehydration reactions, each of which may require unique active sites to increase butene-rich olefin selectivity [7]. The rational design and development of such multifunctional catalysts is essential to achieve industrially relevant ethanol conversions and high C_{3+} olefin selectivity.

Two such multifunctional catalysts for ethanol to C_{4+} olefins formation are Cu-Zn-Y/Beta and Cu-La/Beta catalysts which combine Cu sites for (de)hydrogenation with Lewis-acidic Y/La sites for C-C coupling [16,19]. Cu/La-Beta yields a much higher selectivity toward C_{5+} olefins (~52% over Cu-La$_7$/Beta, 623 K) than Cu/Y-Beta (~ 20% over Cu-Y$_7$/Beta, 623 K), yet both materials catalyze comparable overall C_{3+} olefin yields. This was attributed to an increased selectivity towards further cross aldol condensation between C_4 and C_2 oxygenates relative to dehydration rates over La sites while Y sites preferentially catalyze dehydration over carbon chain growth via further cross condensation. Scheme 1 adapts a previously proposed reaction network [16,19] for forming C_4 aldehyde intermediates from aldol condensation prior to either reduction to butanol and subsequent dehydration to butene or sequential aldol condensation towards C_6 compounds. Influencing the relative rates of these competing reactions by varying catalyst composition and metal selection could significantly impact the alkene product distributions.

Lewis acid sites are the key functional sites for the C-C coupling (aldol condensation) to higher carbon chain olefins such as C_4 or C_{5+} products in the conversion of ethanol as demonstrated in prior studies over both metal oxide- and zeolite-supported catalysts [16–22]. For zeolite-supported catalysts, Lewis acid sites can be generated via isomorphous substitution of heteroatoms into zeolite framework sites. The behavior of Lewis acidic zeolite catalysts such as Zr-Beta, Ta-Beta, and Hf-MFI have been utilized extensively in the ethanol conversion process to catalyze C-C coupling steps [23–25]. Recent studies show that Beta zeolites loaded with rare earth metals are superior to catalyze C-C coupling step in the ethanol upgrading process. For example, Li *et al.* [21] were the first to report that highly dispersed Y species, confined within the microporous environment of Beta zeolites, can effectively enhance the aldol condensation of acetaldehyde derived from ethanol dehydrogenation on Zn centers. In a related study, Bell *et al.* [26] performed detailed structural characterization of Y species and showcased isolated sites grafted onto the zeolite supports. These findings collectively underscore the zeolitic support's capacity to facilitate rare-earth

metal dispersion and generate highly active Lewis acid sites. Davis *et al.* [22] screened a series of bifunctional catalysts supported by silica and zeolite, containing Ag and Ta, Y, Pr, or La, for the ethanol conversion, which marked the initial expansion of the rare-earth metal scope to include La and Pr. It is found that the Lewis acid site with appropriate strength, depending on the type of metal adapted, is the key factor in C-C coupling to the C_{4+} products from ethanol valorization. However, direct comparisons among Lewis acid cations used in the ethanol conversion to C_{3+} olefin products have not been reported.

Here, we investigate the role of rare-earth (RE) metals selection on ethanol conversion to higher C_{3+} products using a series of RE (RE = Y, La, Ce, Gd and Yb) active sites of catalysts. The nature of key intermediates and reaction steps within the cascading reaction network is probed as a function of RE metal identity. Having similar electronic structure but different ion charge density [27], the Y and Lanthanide were chosen to span the lanthanide contraction and give a representative set of ionic radii, which potentially leads to different relative Lewis acidity of RE metals [28]. It's found out that the olefin product distributions can be tailored via adapting different RE metals in bimetallic zeolite catalysts (Cu−RE/Beta), which provides additional flexibility in ethanol conversion to generate useful alkene streams as renewable jet and diesel fuel precursors. Detailed mechanistic investigations on the nature and confining environment of rare earth metals have revealed their impact on reaction rates and alkene selectivity and distribution.

2. Experimental methods

2.1. Catalyst synthesis

Dealuminated Beta (DeAl-Beta) and metal doped DeAl-Beta catalysts were prepared as previously reported procedure [16,19]. DeAl-Beta was obtained by mixing H-Beta Si/Al = 12.5, Zeolyst) with concentrated nitric acid (Sigma Aldrich, >69%) in a perfluoro alkoxy jar (Savillex) at 353 K while stirring for 16 h. The resulting solids were centrifuged and washed repeatedly with DI water and dried overnight at 363 K. Al concentration was measured using inductively coupled plasma atomic emission spectroscopy (ICP-AES), indicating negligible Al concentrations (Si/Al > 1300) in the dealuminated Beta support and subsequently synthesized samples. The bimetallic Cu- and rare earth-doped DeAl-Beta zeolites (Cu-RE/Beta) catalysts were synthesized via solid state grinding. DeAl-Beta was mixed with appropriate masses of copper nitrate trihydrate (Sigma-Aldrich, 98%) and rare earth metal precursor in a mortar and subsequently ground for 20 mins. The well mixed solids were calcined in a tube furnace at 873 K (1 K /min) under air flow (UHP, 100 mL/min) for 6 h. The catalysts were labeled as Cu−RE$_x$/Beta below, where the subscript x indicates the actual RE weight loading obtained from ICP analysis. Monometallic rare earth-doped Beta samples (RE/Beta) were synthesized in a similar procedure.

2.2. Catalyst characterizations

X-Ray diffraction (XRD) patterns were collected on a PANalytical powder diffractometer using CuKα radiation. The working voltage was 40 kV, and the current was 40 mA. The intensity data were collected at
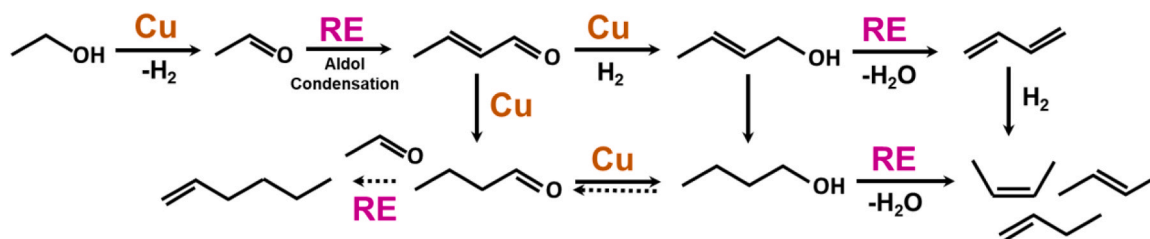
Scheme 1. The outlined reaction pathway for direct conversion of ethanol to C_{3+} olefins [16,19].

room temperature in 2θ range of 4 to 40° at step size of ~0.017°. N_2 adsorption isotherms (77 K) were collected using a Quantachrome Autosorb iQ with ~0.03 g of pelletized and sieved zeolite samples (125–180 μm particle size). Samples were degassed by heating under vacuum (<3 Torr) to 393 K for 1 h and further heating to 623 K for 6 h under vacuum prior to adsorptive analysis. The semilog derivative (δ(Vads/g)/δ(log(P/P0)) vs log (P/P0)) analysis of N_2 adsorption isotherms was used to quantify micropore volumes. Elemental analyses of Cu and rare earth metal loadings were analyzed by inductively coupled plasma atomic emission spectroscopy (ICP-AES) performed at Galbraith Laboratories, Inc.

The morphology and elemental distribution of the catalysts were analyzed by a scanning transmission electron microscopy (STEM), The standards, high resolution (HR) STEM imaging and energy dispersive X-ray spectroscopy (EDS) analysis were performed on an aberration corrected JEOL *JEM-ARM200F NEOARM TEM/STEM* operated at 200 kV with a cold field emission gun (Cold-FEG), a next generation Cs probe corrector (ASCOR) that compensates for higher order aberrations, and EDS system with dual JEOL 100 mm^2 silicon-drift detectors (SDD) for chemical analysis. High resolution analysis was performed with a nominal beam current of ~25 pA and associated resolution of a nominal 0.7 Å. For STEM analysis, the catalysts were drop-cast onto SPI Supplies lacey carbon coated 200 mesh gold 3 mm grids (SPI Supplies part no. 3820 GHCF) from isopropanol suspensions.

X-ray absorption spectroscopy (XAS) was performed at beamline 10-BM and 10-ID of the advanced photon source, Argonne national laboratory to measure the state of Cu and RE (Y, La, Ce, Gd and Yb). Energy calibration was performed simultaneously with sample measurements using a third ion chamber on metal foil standards. Detailed procedures for sample preparation, pretreatment, measurement, and analysis are described in Supporting Information Section S1.

In situ IR spectra of pyridine adsorption on DeAl-Beta and all doped beta zeolites were done in a vacuum transmission IR system. The samples were pretreated at 723 K and then cooled to 393 K for pyridine adsorption. After that, the samples were heated up to 523 K to remove all weakly adsorbed Pyridine and cooled to 393 K to measure strong acid sites.

The temperature programmed desorption of ammonia (NH_3-TPD) was conducted to quantify surface acid site densities and evaluate comparative acid strengths. An Altamira Instruments system (AMI-300) coupled with an online mass spectrometer (OmnistarGSD-301, Pfeiffer Vacuum) was used to perform the TPD measurements. After pretreatment at 823 K for 1 h in 10% O_2/He (50 mL/min), the sample was cooled down to 383 K for ammonia adsorption. The catalyst was exposed to 50 mL/min of 2% NH_3/He for 2 h prior to purging with 50 mL/min of He for 2 h to remove physiosorbed NH_3. Afterwards, the temperature of the sample was ramped from 383 to 1073 K at a rate of 10 K/min, and the NH_3-TPD profile was recorded using the online mass spectrometer (OmniStar GSD-301 (Pfeiffer-Balzer) QMS).

2.3. Ethanol conversion flow reaction

Ethanol conversion experiments were performed in a vertically-aligned quartz reactor (0.5″ OD) at ambient pressure. Catalysts were pelletized, crushed, and sieved (125 to 180 μm for low conversion studies, while 90 −125 μm particle sizes were used for the high conversion studies). prior to being loaded into the reactor between quartz wool beds. Catalysts were pretreated in flowing air (50 mL/min) for 1 h at 673 K, flushed with He (UHP and 50 mL/min), and then reduced in H_2 (UHP and 19.6 mL/min) for 0.5 h at 623 K. Liquid ethanol (Sigma-Aldrich, 99.5%) was fed into the preheated gas mixture using a syringe pump (KD Scientific Legato 180). Products were separated and analyzed using a gas chromatography unit (Agilent 7820 A) equipped with a HP-PLOT-Q column (0.32 mm diameter, 30 m, 20 μm film) and a flame ionization detector (FID). Products were identified via comparison with known standards through a gas chromatograph (Agilent 6850). The

carbon balance for each reaction run is typically 92–96%.

Ethanol conversion and product selectivity of species i were quantified via Equations below:

$$\chi = \left(1 - \frac{\dot{n}_{EtOH,out}}{\dot{n}_{EtOH,in}}\right) \times 100 \tag{1}$$

$$S_i = \frac{n_{C,i}}{n_{C,prod}} \times 100 \tag{2}$$

Here, χ is ethanol conversion, $\dot{n}_{EtOH,in}$ and $\dot{n}_{EtOH,out}$ are the inlet and outlet ethanol molar flow rates, S_i is the selectivity towards species i, $n_{C,i}$ is the moles of carbon in product i, and $n_{C,prod}$ is the combined moles of carbon in all detectable products.

Rate measurements were performed in a low conversion regime (<10% conversion) and typically were measured over 0.01 − 0.05 g of catalyst diluted with 0.8 g of SiC (Alfa Aesar, 120 grit). For experiments using acetaldehyde (Sigma-Aldrich, >99.5%) as a reactant, acetaldehyde was introduced by flowing H_2 through a bubbler at 245 K at ambient pressure. Carbon balances for low conversion measurements are ~100% but drop to 92–96% for high conversion measurements. Butanol dehydration measurements fed liquid butanol into the reactor in an analogous way to liquid ethanol feeding. A one-site exponential function was used to fit the transient kinetic profile when feeding acetaldehyde or butanol, and the initial C−C coupling or dehydration rate was calculated by extrapolating to initial times [29,30].

3. Results and discussion

3.1. Physical properties and structural characterization of as-synthesized monometallic (RE/Beta) and bimetallic (Cu-RE/Beta) catalysts

Cu and rare earth metal densities were analyzed by ICP-AES for all samples and are listed in Table 1 (bimetallic samples) and Table S1 (monometallic samples). The Cu loading is maintained at ~0.9 wt% for all bimetallic samples, and the RE loading is in the range of 0.7–0.8 mmol/g for both bimetallic and monometallic samples. ICP results suggested that the actual concentration of doped RE metals is consistent with the nominal loading in the starting materials for all samples (Table 1 and Table S1). The Cu loading is comparable for all the bimetallic samples and the RE metal concentration for bimetallic samples was kept at a similar mole concentration. Likewise, each monometallic sample contains similar RE metal content.

The texture structural properties of DeAl-Beta, RE/Beta and Cu-RE/Beta were measured by N_2 adsorption-desorption isotherms (Fig. S1). The BET surface area and pore volume (Table 1) derived from adsorption branch of N_2 isotherms are consistent with the parent Beta zeolite although both surface area and micropore volume are decreased after loading metals. As indicated in our previous work [16,19], the decrease in micropore volumes and surface area at high metal loadings could be attributed to the partial pore blockage by the metal species.

Fig. 1 shows measured XRD patterns of H-Beta, DeAl-Beta, monometallic RE/Beta, and bimetallic Cu-RE/Beta catalysts investigated in this work, which showed that the primary BEA structure was well preserved after dealumination and sequential introduction of metals, in agreement with micropore volumes derived from N_2 adsorption isotherms. This suggests that neither dealumination nor the introducing of Cu or rare earth metals changes the structural parameters of zeolite support significantly. Except for Ce-based samples, XRD measurements did not show any evidence of Cu and rare earth metal related species, demonstrating that the doped metals are either well dispersed or present as non-crystalline species in the zeolite possibly due to their interaction with the silanol groups generated by the removal of Al [16,19]. For both Cu-Ce/Beta and Ce/Beta samples, the weak and weak peaks are likely from partially crystallized CeO_x, indicating that a small portion of Ce species exist as small nanoparticles in the Ce doped samples. These findings are corroborated by STEM images and corresponding EDS

Table 1
BET surface areas, pore volumes, and metal loadings for DeAl-Beta and all Cu-RE/Beta samples studied here.

Samples	Surface area[a] (m²/g)	Total pore[b] volume (cm³/g)	Micropore volume (cm³/g)	Cu weight percent (wt%)	RE weight percent (wt%)	Cu molar loading (mmol/g)	RE molar loading (mmol/g)
DeAl-Beta	530	0.69	0.20	-	-	-	-
Cu-Y₇/Beta	401	0.49	0.15	0.9	6.7	0.14	0. 76
Cu-La₁₂/ Beta	418	0.52	0.15	0.9	11.8	0.14	0.84
Cu-Ce₁₀/ Beta	454	0.54	0.16	0.9	9.6	0.15	0.70
Cu-Gd₁₂/ Beta	458	0.61	0.17	0.9	12.1	0.15	0.76
Cu-Yb₁₂/ Beta	451	0.53	0.16	0.9	12.3	0.14	0.71

[a] Calculated from multipoint BET method.
[b] Calculated from the volume of adsorbed nitrogen.
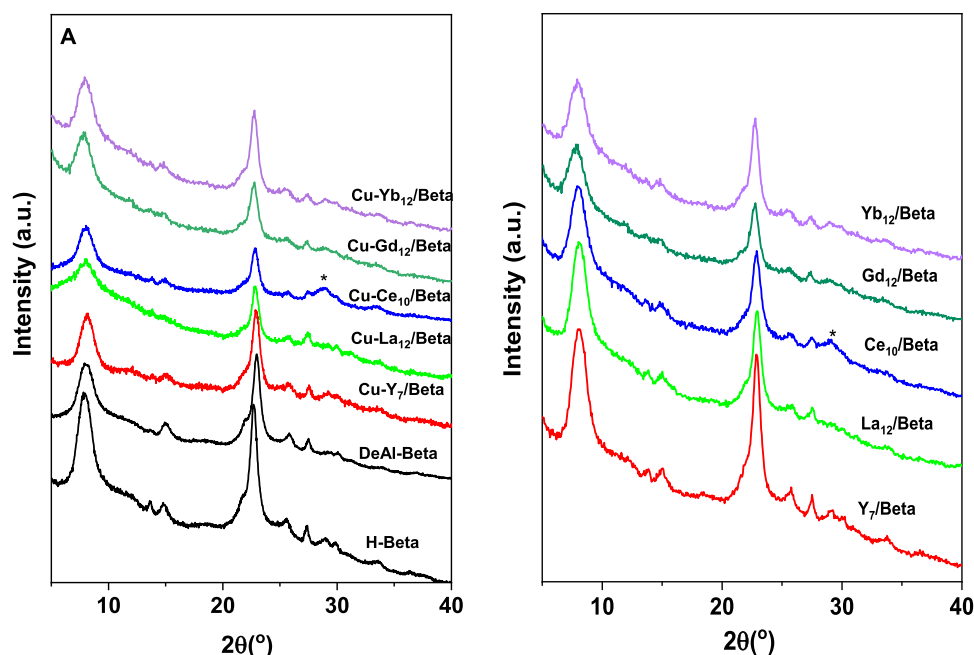
Fig. 1. XRD diffraction patterns for A) H-Beta, DeAl-Beta and Cu-RE/Beta; B) RE/Beta samples. (* XRD peak for CeOₓ).

measurements (Fig. 2). Small areas of bright contrast in the STEM images of Cu-Ce₁₀/Beta indicate CeOx nanoparticles (Fig. 2C and Fig. S2), which supports the interpretation of XRD patterns (Fig. 1) for Ce containing catalysts. In other Cu-RE/Beta catalysts, RE$_x$O$_y$ particles are not observed in the STEM images and element maps, indicating each RE element overall is homogenously dispersed through the Beta zeolite support for other Cu-RE/Beta samples. The High-angle annular dark-field (HAADF) STEM images and elemental EDS maps indicate the uniform distribution of Cu as isolated sites in all bimetallic Cu-RE catalyst particles. Based on the high dispersion suggested by STEM images and XRD, XAS was used to further understand the local structure of Cu and RE metals in the catalysts.

Metal oxidation states and the local coordination environment were investigated by XAS at the RE L₃ (La, Ce, Gd and Yb) or K (Cu and Y) edge on the RE-containing Beta materials. Fig. 3A shows the Cu K edge X-ray absorption near edge structure (XANES) for as-synthesized Cu-RE/ Beta catalysts alongside reference spectra for CuO (Cu²⁺), Cu₂O (Cu¹⁺), and copper foil (Cu⁰). All Cu-RE/Beta catalysts have closely matching spectra, indicating a similar local order around Cu in the series. The edge energy of all bimetallic catalysts aligns with that of CuO, demonstrating that copper is in the + 2 oxidation state. In addition, all as-synthesized catalysts have a pre-edge peak at 8979 eV, consistent with Cu²⁺. Compared to CuO, the shape of the ligand to metal charge transfer

(LMCT) peak and the white line (Fig. 3B) are distinct, reflecting changes in the local environment around copper on the respective catalysts. EXAFS spectra (Fig. 3B) uniformly showed a Cu-O scattering in the first shell and a weak 2nd shell. EXAFS modelling of the series yielded a Cu-O coordination number (CN) of close to 4 across the series, consistent with tetrahedrally coordinated copper (Table S3). A consistent EXAFS model was utilized across the range of Cu-RE/Beta sample series (Fig. S3 and Table S3), and no samples show discernible Cu-Cu scattering peaks from either Cu metal (2.24 Å, phase uncorrected) or Cu oxide (CuO: 2.51, 2.92 Å Cu₂O: 2.69 Å phase uncorrected), indicating that Cu sites on individual bimetallic catalyst are highly dispersed. Second shell scattering across the series was modeled using Cu-Si scattering, which is consistent with a single site Cu structure. Cu K edge spectra could not be collected on Cu-Yb/Beta due to the overall of the Cu K edge (8979 eV) and the Yb L₃ (8944 eV) EXAFS.

XAS data were also collected on each RE-containing sample at the corresponding RE L₃ edge. Fig. 4 depicts XAS spectra collected on Yb/ Beta and Cu-Yb/Beta at the Yb L₃ edge as an example. Fig. 4A shows consistent XANES edge energies for Yb/Beta, Cu-Yb/Beta, and Yb₂O₃, indicating a consistent + 3 Yb oxidation state across all samples. Compared to Yb₂O₃, the whiteline peak intensity of Cu-Yb/Beta and Yb/ Beta samples are higher (Fig. 4B), suggesting that Yb in the catalysts has a different coordination symmetry of the oxygen environment or a
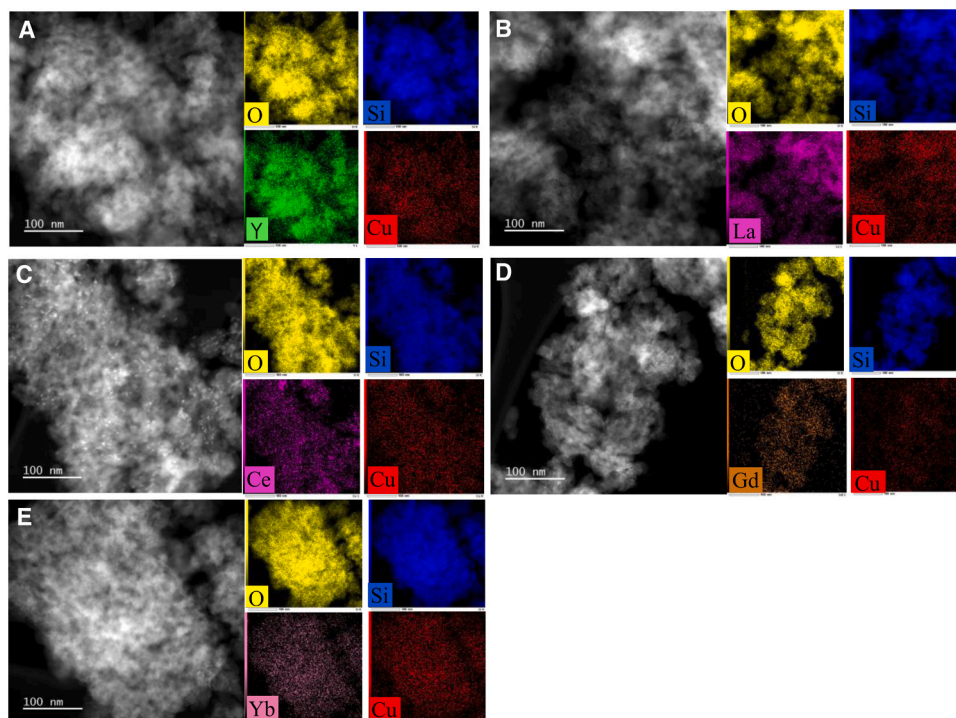
Fig. 2. STEM image with corresponding EDX elemental maps of Cu and RE metals for bimetallic Cu-RE/Beta catalysts: A) Cu-Y$_7$/Beta, B) Cu-La$_{12}$/Beta, C) Cu-Ce$_{10}$/beta, D) Cu-Gd$_{12}$/Beta, E) Cu-Yb$_{12}$/Beta.
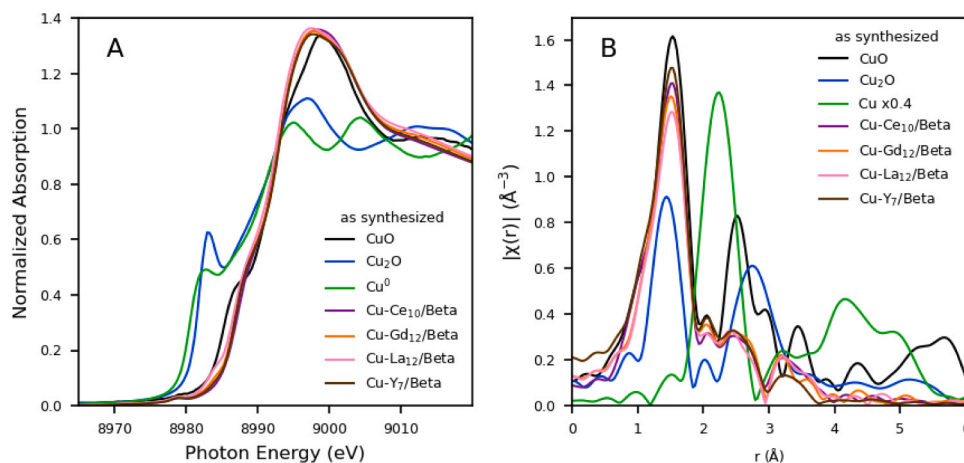
Fig. 3. Cu K edge XAS spectra of Cu-RE/Beta along with Cu oxide and Cu foil references (A) XANES spectra (B) R space EXAFS spectra.

different coordination number. In addition, Yb$_2$O$_3$ also has a post edge peak at 8965 eV that is not present in the Yb-doped Beta spectra (Fig. 4A). Yb L$_3$ edge R-space EXAFS spectra (Fig. 4B) of Cu-Yb/Beta and Yb/Beta catalysts show that the two samples have similar Yb structures at the same measurement conditions. The Yb-O scattering peak between 1–2.5 Å (phase uncorrected) is broader and lower in intensity compared to Yb$_2$O$_3$ (Fig. 4B). Yb$_2$O$_3$ has a strong 2nd shell between 2.5–4 Å (phase uncorrected) from Yb-Yb scattering at a bond distance of 3.46 and 3.94 Å. In contrast, the catalysts have a weak 2nd shell scattering peak between 2.5–3.5 Å (phase uncorrected) that is different in shape compared to Yb$_2$O$_3$, which rules out a Yb$_2$O$_3$ nanoparticle structure in the material. Instead, the weak scattering likely results from a lower Z neighbor such as Si. The broad, weak 2nd shell reflects a configurationally complex bonding structure and is consistent with highly dispersed Yb on the zeolite surface.

Similar analyses were performed for all other RE-containing samples

at their corresponding RE L$_3$ edges (Fig. S4). XANES edge energies of all other RE and Cu-RE samples shows that the RE cations are in oxidation states corresponding to their bulk oxides (Ce^{+4} for Ce, RE^{+3} for all others). For all samples, the RE-O scattering peak is lower in intensity and broader than that of the corresponding crystalline oxide, indicating higher static disorder in the RE-O bond distance distribution and/or a different RE-O coordination number. With the exception of the Ce-containing samples, all Cu-RE/Beta and RE/Beta materials have weaker 2nd shell peaks and shorter RE-RE bond distances than in their corresponding oxides (Fig. S4). This again suggests the presence of a lower Z neighbor such as silicon. Therefore, the EXAFS is consistent highly dispersed RE species on all Ce-free samples studied here. However, based on the similar shapes of the Ce 2nd shell of CeO$_2$ and Ce-containing samples (Fig. S4f), some Ce on Cu-Ce$_{10}$/Beta and Ce$_{10}$/Beta are present as small CeO$_2$ agglomerates, mirroring XRD and microscopy results. Overall, these as-synthesized samples primarily possess highly
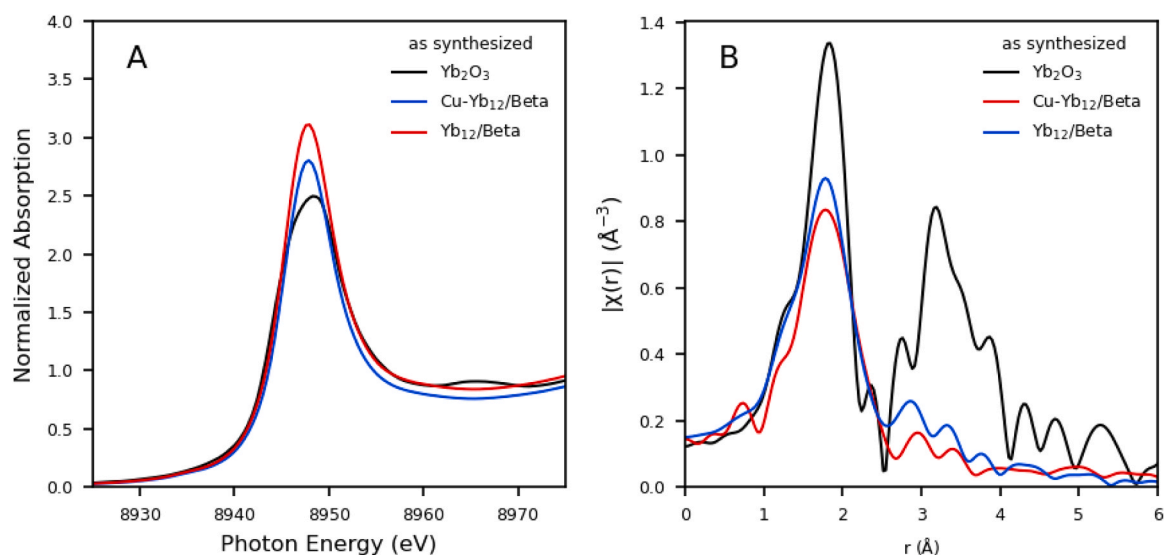
Fig. 4. Yb L$_3$ edge XAS spectra of Yb/Beta and Cu-Yb/Beta along with Yb$_2$O$_3$ references (A) XANES spectra (B) R space EXAFS spectra.

dispersed Cu and RE sites for bimetallic Cu-RE/Beta samples as well as well-dispersed RE sites for monometallic RE/Beta samples.

EXAFS modeling of the RE-O local structure was used to estimate the ionic-radius of RE elements in the Cu-RE/Beta and RE/Beta catalyst series. Based on the fit total RE-O coordination number, the ionic radius can be determined based on tabulated values for a given coordination number and valence. Table 2 lists the total RE-O coordination number, its valence (based on XANES analysis) and the calculated ionic radius based on reference [31]. The results follow the trend of the lanthanide contraction, with La having the largest ionic radius, and Yb having the smallest. The ionic radius of Y is close to that of Yb with slightly smaller ionic radius. Notably, all RE elements have a total RE-O coordination number higher than 4, which would be the case if the RE elements isomorphically substituted into the zeolite framework. Given that the ionic radius tetrahedral Al^{3+} is 0.39 Å it is unsurprising that the RE elements, which have more than two times the Al radius, do not substitute into the lattice the way other cations (Ti, Sn etc.) are known to do. Based on the ionic radii, La would be predicted to be the softest Lewis acid in the catalyst, while Yb would be predicted to be the hardest, which is consistence with the trend reported in literature [28].

3.2. Impact of catalyst composition on ethanol upgrading catalysis

The Cu-RE/Beta materials were first examined for ethanol-to-olefins conversion at high ethanol conversions. Fig. 5 depicts pseudo steady-state product distributions from ethanol conversion in hydrogen gas (623 K, 3–5 h time-on-stream). All tested bimetallic samples catalyze > 80% C$_{3+}$ olefin selectivity at ~100% ethanol conversion. The primary products are butene isomers and C$_{5+}$ alkenes with acetaldehyde, ethylene, propene, and water making up less than 10% of the total carbon yields (Table S2). Notably, distinct shifts in relative selectivity to butene and C$_{5+}$ alkenes are observed over Cu-RE/Beta catalysts as a

function of RE metal identity. Cu−La$_{12}$/Beta exhibited the highest C$_{5+}$ selectivity (48.8%) while the Cu-Yb$_{12}$/Beta gave the highest butene selectivity around 63.1% despite similar ethanol conversion and overall C$_{3+}$ alkene selectivity. The sequence of butene/C$_{5+}$ olefin ratio is Cu-Yb$_{12}$/Beta (3.4) > Cu-Y$_7$/beta (3.1) > Cu-Gd$_{12}$/Beta (2.2) > Cu-Ce$_{10}$/Beta (1.2) > Cu−La$_{12}$/Beta (0.73).

As proposed in Scheme 1 above, Cu and RE metal sites primarily catalyze separate reactions within the cascading ethanol-to-olefins reaction network. Cu sites have been previously observed to primarily catalyze ethanol dehydrogenation and unsaturated C$_{4+}$ aldehyde/alcohols hydrogenation [16,19] and therefore will have a diminished effect on observed olefin distribution. La and Y sites have been correlated with aldol condensation reactivity and as primary dehydration active sites at similar reaction conditions. Since product distributions summarized in Fig. 5 indicate > 80% C$_{3+}$ alkene formation over all bimetallic catalysts investigated here, it is reasonable to assign the RE metal centers as the primary aldol condensation and dehydration active sites for each of these materials as well. This will be further investigated below over monometallic RE/Beta samples. Changes in alkene product distributions towards either butene isomers or longer carbon chain (C$_{5+}$) products can therefore be correlated with either the varied RE metal identity or RE active site speciation across the range of samples. Based on the characterization data presented above, similar bulk distributions of RE metals can be reasonably assumed, suggesting that differences may be attributable to RE metal identity given the absence of specific active site quantifications. To investigate this further, the nature and acid sites quantity of RE metal centers and their unique aldol condensation and dehydration rates will be measured.

3.3. The dependence of reaction rate on rare earth metal identity over RE/Beta catalysts

As mentioned above, monometallic RE/Beta catalysts containing similar RE metal loadings, XAS behavior, and bulk metal dispersions relative to their bimetallic counterparts have been synthesized to further understand how the varied RE metal identity and associated Lewis acidity affects the ethanol-to-olefin reaction rates. The nature and strength of the Lewis acid sites in the RE/Beta samples were first investigated using IR spectroscopy with pyridine as a probe molecule. The transmission IR spectra were collected on DeAl-Beta and monometallic RE/Beta at 393 K after evacuated at 723 K after saturation with pyridine at 393 K (Fig. 6) to detect the acid sites generated by rare earth metal incorporation.

Table 2

RE cation valence, RE-O coordination number, and ionic radius of Cu-RE/Beta catalysts.

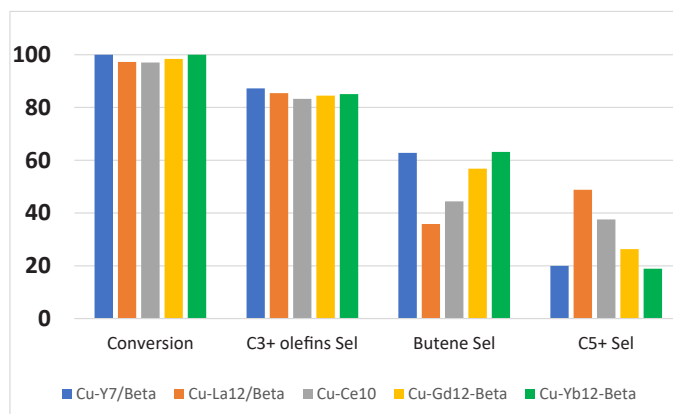| Catalyst	RE Valence	RE-O CN*	Ionic radius (Å)
Cu-La/beta	La^{3+}	7.6	1.16
Cu-Ce/beta	Ce^{4+}	8.0	0.97
Cu-Gd/beta	Gd^{3+}	6.8	1.00
Cu-Y/beta	Y^{3+}	6.0	0.90
Cu-Yb/beta	Yb^{3+}	5.7	0.87

* Coordination number

Fig. 5. Ethanol conversions and olefin product selectivities over bimetallic Cu-RE/Beta catalysts (623 K, 6.8 kPa ethanol, 99 kPa H_2, WHSV: 0.53 h^{-1}). The relative errors in conversion and selectivity are 5%.
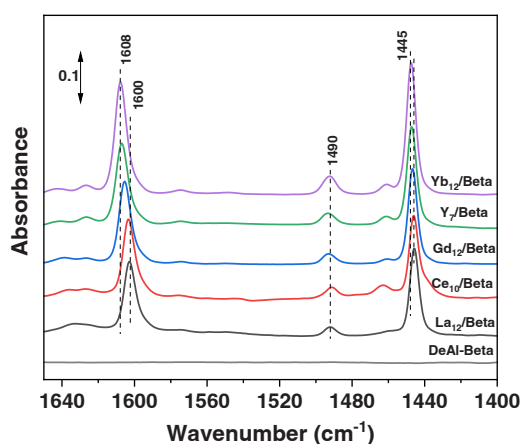

Fig. 6. Transmission IR spectra collected on DeAl-Beta and all monometallic RE/Beta samples at 393 K after evacuated 723 K after pyridine saturation at 393 K.

The spectra of each RE/Beta sample has two bands centered at approximately 1600–1608 and 1445–1449 cm^{-1} which are not present in the DeAl-Beta support; these bands are attributed to the ν8a and ν19b modes of pyridine coordinated to Lewis acid sites [32–34]. No IR bands were observed at ~1540 cm^{-1} reflecting protonated pyridine caused by adsorption onto Brønsted acid sites [33–35]. This indicates that the incorporation of rare earth metal generates Lewis acid sites, but does not mean that all RE metal centers are Lewis acidic. The peak at 1491 cm^{-1} is the overlap of the Brønsted and Lewis acid sites [36]. In this study, due to the absence of the Brønsted acid sites across all RE/Beta catalyst, the peak should be assigned to the Lewis acid sites. Typically, the ν8a mode of physically adsorbed pyridine is reflected by a peak centered at 1580 cm^{-1} [37], and this peak shifts to higher wavenumbers when pyridine is adsorbed on Lewis acid sites where the degree of shift reflects the strength of the Lewis acid sites. In general, the peak reflecting the ν8a mode increases to higher wavenumbers with increasing Lewis acid strength. Fig. 6 shows that the ν8a mode bands observed from pyridine adsorbed onto the monometallic RE/Beta shifts to progressively higher wavenumbers (1600 to 1608 cm^{-1}) in the following order: La_{12}/Beta, Ce_{10}/Beta, Gd_{12}/Beta, Y_7/Beta, Yb_{12}/Beta. This suggests that the Lewis acidic Yb sites on Yb_{12}/Beta possess the strongest Lewis acidity while the Lewis acidic La sites on La_{12}/Beta possess the weakest Lewis acidity. The similar trend is observed at ν19b mode bands, which shifts from 1445 to 1449 cm^{-1}.

NH_3-TPD was performed to get the further information about the nature and strength of acid sites for RE/Beta samples. NH_3-TPD profiles

(Fig. S5) showed a broad peak with maxima at around 493 K for all RE/Beta samples, corresponding to ammonia desorption from Lewis acid sites [38,39], which was not observed for DeAl-Beta sample. There is negligible desorption noticed at high temperatures (above 673 K) to the Brønsted acidic site for all RE/Beta samples [39]. This affirms the IR results from pyridine adsorption that the rare earth metals are the Lewis acid centers in this catalytic system. Secondary desorption peaks at around 603 K are clearly discernible for Ga_{12}/Beta, Y_7/Beta and Yb_{12}/Beta, and the corresponding peak maxima shifts towards higher temperatures in the order of Ga_{12}/Beta $< Y_7$/Beta $< Yb_{12}$/Beta. This suggests that these three RE/Beta samples possess two different type of Lewis acidic sites which could have distinctive Lewis acid strengths. Considering that the NH_3 desorption over Ce_{10}/Beta sample is about 40 K higher than La_{12}/Beta, the Lewis acid strength follows the sequence of La_{12}/Beta $< Ce_{10}$/Beta $< Gd_{12}$/Beta $< Y_7$/Beta $< Yb_{12}$/Beta, in agreement with the IR observations in Fig. 6. Notably, the trend of Lewis acidic strength of RE/Beta catalyats is in line with the ionic radius (long to short) of RE species in Beta zeolites as derived from EXAFS modeling of RE-O local structure. This is also in agreement with work reported in literature [40]. Yoon et al. have elucidated the linear dependence of surface Lewis acidic of RE ions on Sandersons Electronegativity values, which is in line with the electron number density of RE ions, directly correlating with the ionic radius of elements. In addition, there is only one type of Lewis acid site observed for all RE/Beta samples from IR pyridine adsorption measurement, which likely due to the strong base nature of pyridine that is not sensitive enough to discriminate multiple types of Lewis-acid sites with similar local coordination for individual rare earth metal. Thus, the IR results presented average acidic property for all RE/Beta samples.

The quantitative analysis of IR-pyridine adsorption and NH_3-TPD measurements for the surface density of Lewis-acidic RE sites across a series of monometallic samples is listed in Table 3. Quantification of the NH_3 TPD profiles indicate very similar desorbed NH_3 quantities.

per gram of catalyst across the RE/Beta samples (~5% variation),

Table 3
Surface density of Lewis acid RE sites on monometallic RE/Beta samples.

	Y_7/ Beta	La_{12}/ Beta	Ce_{10}/ Beta	Gd_{12}/ Beta	Yb_{12}/ Beta	DeAl- Beta
1445 cm^{-1} (Pyridine IR) Lewis acidic Density (cm^{-1}.g^{-1})	182	175	163	183	181	0
Density of Lewis acidic sites (NH_3-TPD) (µmol/g)	584.5	577.9	558.4	577.0	575.2	0

indicating the surface number of Lewis acid sites is consistent for all RE/Beta samples. These counts reflect the total integrated peak area from the primary desorption peak (~493 K) and the shoulder peak (~603 K).

Due to the lack of reported integrated molar extinction coefficients (IMECs) for pyridine over Lewis acidic RE sites, integrated peak areas (for the peak centered at 1445 cm^{-1}) normalized by catalyst wafer mass, were used to allow comparisons of the Lewis-acidic RE sites density across RE/Beta samples (Table 3). The concentration of Lewis acid sites based on the pyridine-IR analysis is comparable over all RE/Beta samples, which affirms the results from NH3-TPD. Lewis acidic site counts on Ce$_{10}$/Beta are slightly lower (~ 5%) compared with the other RE/Beta, possibly due to the presence of some CeO$_x$ nanocluster species as previously observed via XRD, STEM and XAS.

On the basis of acid site studies via IR-pyridine and NH$_3$-TPD, it is found that the butene/C$_{5+}$ olefin ratio in product stream of ethanol conversion (Fig. 5) over bimetallic Cu-RE/Beta catalysts are increased with increasing strength of Lewis acid RE sites, which is closely correlated with the ionic radius of RE elements in catalysts.

With these characterizations in mind, the role of the RE metal on the overall ethanol conversion reaction network can be probed. According to the reaction network proposed in Scheme 1, crotonaldehyde is formed via aldol condensation of acetaldehyde dimers, and can be hydrogenated to butyraldehyde, reduced via MPV reduction to crotyl alcohol or condensed with an additional acetaldehyde to form a C$_6$ aldehyde. Butene isomers are then produced from either the dehydration of crotyl alcohol and subsequent selective hydrogenation or the reduction of butyraldehyde to 1-butanol and subsequent dehydration. According to our previous work [19], the presence of Cu sites in our catalysts favors hydrogenation of the crotonaldehyde C=C bond, leading to remarkably higher selectivity toward butyraldehyde relative to crotyl alcohol under the hydrogen environment. Therefore, the 1-butanol dehydration pathway is dominant for butene isomers formation in the abundance of H$_2$. The hydrogenation/dehydrogenation reactions between aldehyde and alcohol in the reaction network are reversible steps [40] and are not rate determining steps for carbon chain growth from C$_4$ intermediates as indicated previously [19] and butanol dehydrogenation rate measurement (Fig. S6). Taken together, the relative rate of C-C coupling (C$_4$ aldehyde further condensation) and C$_{4+}$ alcohol (1-butanol) dehydration reaction will play an important role on the selective formation of butene or C$_{5+}$ olefins.

To investigate the impact of RE metal identity on ethanol upgrading chemistry, reaction rates for C-C coupling and C$_{4+}$ alcohol dehydration were investigated at low conversions (<10%) over the monometallic RE/Beta catalysts. Acetaldehyde coupling and 1-butanol dehydration were probed as model reactions within the larger ethanol conversion reaction network and are correlated with carbon chain growth and

termination steps in the proposed reaction network (Scheme 1). Fig. 7 A shows transient aldol condensation rates to form crotonaldehyde from acetaldehyde over the monometallic RE/Beta catalysts. Transient rates were fit using a single site exponential decay model and extrapolated back to initial times. Initial C−C coupling rates normalized by the mole of RE metal sites are plotted in Fig. 8 and are 1.5, 1.7, 1.8, 1.9 and 2.0 mmol (mol$_{RE}$ s)$^{-1}$ for La$_{12}$/Beta, Ce$_{10}$/Beta, Gd$_{12}$/Beta, Y$_7$/Beta and Yb$_{12}$/Beta, respectively. The trend is consistent with the strength of Lewis acid RE sites detected by IR spectroscopy and NH$_3$-TPD, suggesting that increased Lewis acid strength facilitates the C-C coupling reaction (Fig. 7 A). This could be due to several phenomena such as an increased adsorption enthalpy of the acetaldehyde reactant onto the stronger Lewis acid sites or a higher acetaldehyde coverage on stronger Lewis acid sites. However, shifts in C-C coupling rates are not large as a function of RE metal identity.

Initial butanol dehydration rates were obtained in a similar fashion to C-C coupling rates (Fig. 7B) and increase over the same ordering of RE/Beta catalysts: 0.8, 2.4, 3.5, 4.9 and 6.5 mmol (mol$_{RE}$ s)$^{-1}$ (Fig. 8) for La$_{12}$/Beta, Ce$_{10}$/Beta, Gd$_{12}$/Beta, Y$_7$/Beta and Yb$_{12}$/Beta, respectively. Notably, though both C-C coupling rate and butanol dehydration rate systematically increase with increasing RE Lewis acid strength (characterized by the shift degree of ν8a mode band), the differences in
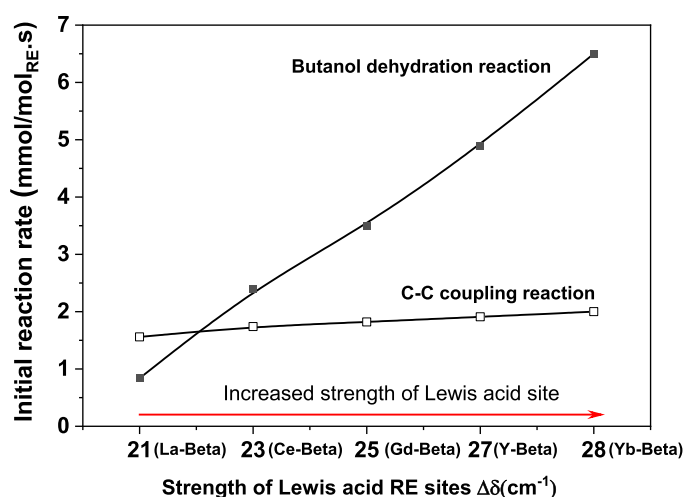

Fig. 8. The initial rate of C-C coupling rate and butanol dehydration rate are plotted in order of Lewis acidity linked to incorporated RE metals. ((reaction condition for C-C coupling: 543 K, 1.1 kPa acetaldehyde, 115.1 kPa H$_2$, WHSV=11 h^{-1}; reaction condition for butanol dehydration: 543 K, 4.2kPa Butanol, 117.9 kPa H$_2$, WHSV= 14 h^{-1}).
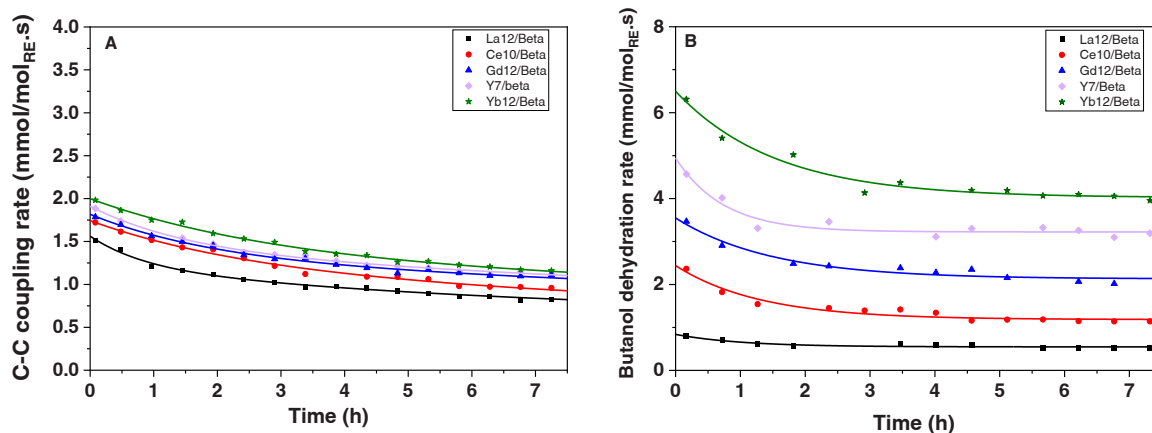

Fig. 7. (A) C-C coupling rate and (B) Butanol dehydration rate over monometallic RE/Beta catalysts (reaction condition for C-C coupling: 543 K, 1.1 kPa acetaldehyde, 115.1 kPa H$_2$, WHSV=11 h^{-1}; reaction condition for butanol dehydration: 543 K, 4.2kPa butanol, 117.9 kPa H$_2$, WHSV= 14 h^{-1}).

reaction rates as a function of RE identity are significantly larger for butanol dehydration than for acetaldehyde coupling (Fig. 8). In other words, butanol dehydration appears more sensitive to RE Lewis acid strength than aldol condensation. Importantly, except for La$_{12}$/Beta catalyst, the monometallic RE/Beta catalysts showed higher performance for butanol dehydration relative to aldol condensation (1.4, 1.9, 2.6 and 3.3 times higher over Ce$_{10}$/Beta, Gd$_{12}$/Beta, Y$_7$/Beta and Yb$_{12}$/ Beta, respectively, Fig. 8). In contrast, the C-C coupling rate (1.5 mmol mol$_{La}$s^{-1}) is 1.9 times higher than butanol dehydration rate (0.8 mmol mol$_{La}$s^{-1}) over La$_{12}$/Beta catalyst. Taken together within the context of the ethanol conversion reaction network, these findings suggest that the highest butene selectivity can be observed over Cu-Yb$_{12}$/Beta due to the Yb sites possessing the highest ratio of butanol dehydration to C-C coupling rate. Similarly, Cu-La$_{12}$/Beta should facilitate the highest selectivity towards C$_{5+}$ olefins as the La sites promote the formation of longer carbon chain olefins (C$_{5+}$) due to favoring further C-C coupling reaction from C$_4$ intermediates over the C$_4$ alcohol dehydration. The lower butanol dehydration rate leads to the higher butanol intermediate presenting in the reactor. Since butanol dehydrogenation to butyraldehyde is reversible step [19], the C$_4$ intermediate should be prolonged to stay in the reactor, promoting further cross condensation reaction to form C$_{6+}$ products. Ethanol conversion product distributions measured over the other Cu-RE/Beta materials would then fall between these two bookend catalysts and would increasingly favor butene formation with each RE metal's preferential selectivity towards dehydration over aldol condensation.

Since the acetaldehyde condensation and butanol dehydration reflect the nature of RE Lewis acid sites included in the catalysts, essentially related to the ionic radius of RE elements loaded in Beta zeolite, to quantitively understand the relationship between product distribution and Lewis acid RE sites, the fraction of butene to C$_{5+}$ olefins in the product stream over bimetallic Cu-RE/Beta (Fig. 5) was plotted with the ionic radius of RE species, characterizing the strength of Lewis acid RE sites, as well as the relative ratio of initial reaction rate of butanol dehydration to C-C coupling as shown in Fig. 9. A linear dependence of butene/C$_{5+}$ olefins ratio in product stream as a function the strength of Lewis acid RE sites (ionic radius of RE species) is simultaneously in line with the initial rate of butanol dehydration to C-C bond formation. The relative ratio of C$_4$/C$_{5+}$ alkene products reflects the competition between further aldol condensation of C$_4$ aldehydes with

additional acetaldehyde and dehydration reactions of the C$_4$ alcohol and increases from 1.1 to 3.3 as the ratio of butanol dehydration and C-C coupling rates rises above 1.4 (Fig. 8), which is linked with increased Lewis acidity from the Ce- to Yb-containing catalysts. In contrast, bimetallic Cu-RE/Beta catalysts with butanol dehydration to C-C coupling rate ratios below 1.4 shift the olefin product distribution to higher C$_{5+}$ product yields (Fig. 8). This further confirms that the variations of Lewis acidic RE sites are the key factor to alter the product distribution associated with the butene/C$_{5+}$ olefins ratio. Note the Ce-based sample is slight off the trend in Fig. 9 for ionic radius dataset. The Ce-based samples are present as mixture of CeO$_2$ nanoparticles and single sites characterized by STEM and XAS. Given the complication of EXAFS modeling, the ionic radius of Ce element is derived from EXAFS modeling based on CeO$_2$ nanoparticle only, which would lead to the potential error bar on the calculation of ionic radius of Ce element. This could be the reason that Ce-based sample is drifted from trend line.

Besides the apparent significance of Lewis acidic RE sites detected by transmission IR-pyridine and NH$_3$-TPD, we cannot completely rule out the contributions from other types of RE sites that do not bind pyridine and NH$_3$ strongly and thus cannot be directly probed by FTIR spectroscopy or NH$_3$-TPD measurements. It is also challenging to provide further insights into the coordination environment of the rare earth metal sites to distinguish the type of Lewis acidic sites relevant to reaction kinetics from XAS due to the complicated spectra.

3.4. Temperature effect on catalyst performance for ETO reaction

To further understand the reaction pathways presented in ethanol upgrading over the bimetallic Cu-RE/Beta catalysts and the impact of the RE metal ions, ethanol conversion and C$_{3+}$ olefin selectivity were further studied by varying the reaction temperature. As shown in Fig. 10, reaction temperatures were studied from 473 to 723 K to optimize catalyst performance while holding other reaction conditions constant (7.5 kPa ethanol, 99.3 kPa H$_2$, WHSV 0.52 h^{-1}). Similar product distributions were observed across the series of Cu-RE/Beta catalysts at any given temperature investigated here. Ethanol conversion was increased monotonically from ~10% to 100% as temperature was ramped up to 623 K for Ga, Y and Yb-based catalysts or 673 K for Ce and La-based catalysts after which complete ethanol conversion is maintained. C$_{3+}$ olefin selectivity is maximized (80–88%) at 100% ethanol conversion at 623 K over all Cu-RE/Beta catalysts. As the temperature is increased to above 673 K, acetaldehyde selectivity decreases as ethanol is dehydrated to ethylene instead. Interestingly, the formation of C$_{5+}$ olefins is favored over butene below 573 K for all measured catalysts, yet butene becomes the major product in the C$_{3+}$ olefin stream at increased temperatures (above 573 K over Cu-Yb$_{12}$/Beta, Cu-Y$_7$/beta and Cu-Gd$_{12}$/Beta and above 623 K over Cu-La$_{12}$/Beta and Cu-Ce$_{10}$/ Beta). Maximized butene selectivity is achieved at 623 K over samples containing RE sites with higher dehydration selectivity (Cu-Yb$_{12}$/Beta, Cu-Y$_7$/beta and Cu-Gd$_{12}$/Beta) while similar behavior is observed at 673 K over Cu-La$_{12}$/Beta and Cu-Ce$_{10}$/Beta catalyst. This reflects differences in relative rates for dehydration and aldol condensation over these RE metals which are likely caused by activation energy differences that favor dehydration at higher temperatures. In summary, lower temperatures favor C$_{5+}$ olefin formation while higher temperatures favor butene selectivity over these Cu-RE/Beta catalysts.

As reported in the literature [7], the aldol condensation reaction is exothermic, therefore condensation of acetaldehyde to crotonaldehyde and further cross aldol condensation can be efficiently realized at lower temperatures. However, the dehydration of alcohol is slightly endothermic, which is more dependent on reaction temperature. The C$_4$ alcohol dehydration reaction is limited at low temperatures over Cu-RE/Beta catalysts, as evidenced by significant 1-butanol formation below ~520 K (Fig. S7), which led to the C$_{5+}$ olefin formation from further cross condensation between the prolonged C$_4$ aldehyde intermediate with an additional acetaldehyde. Butanol is completely
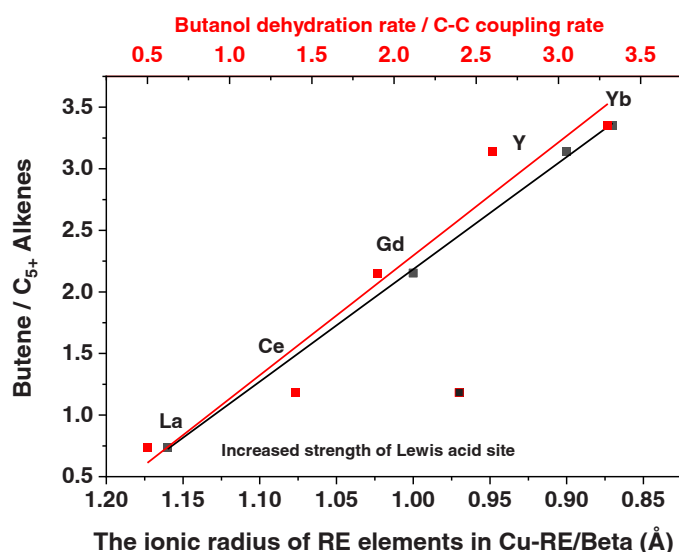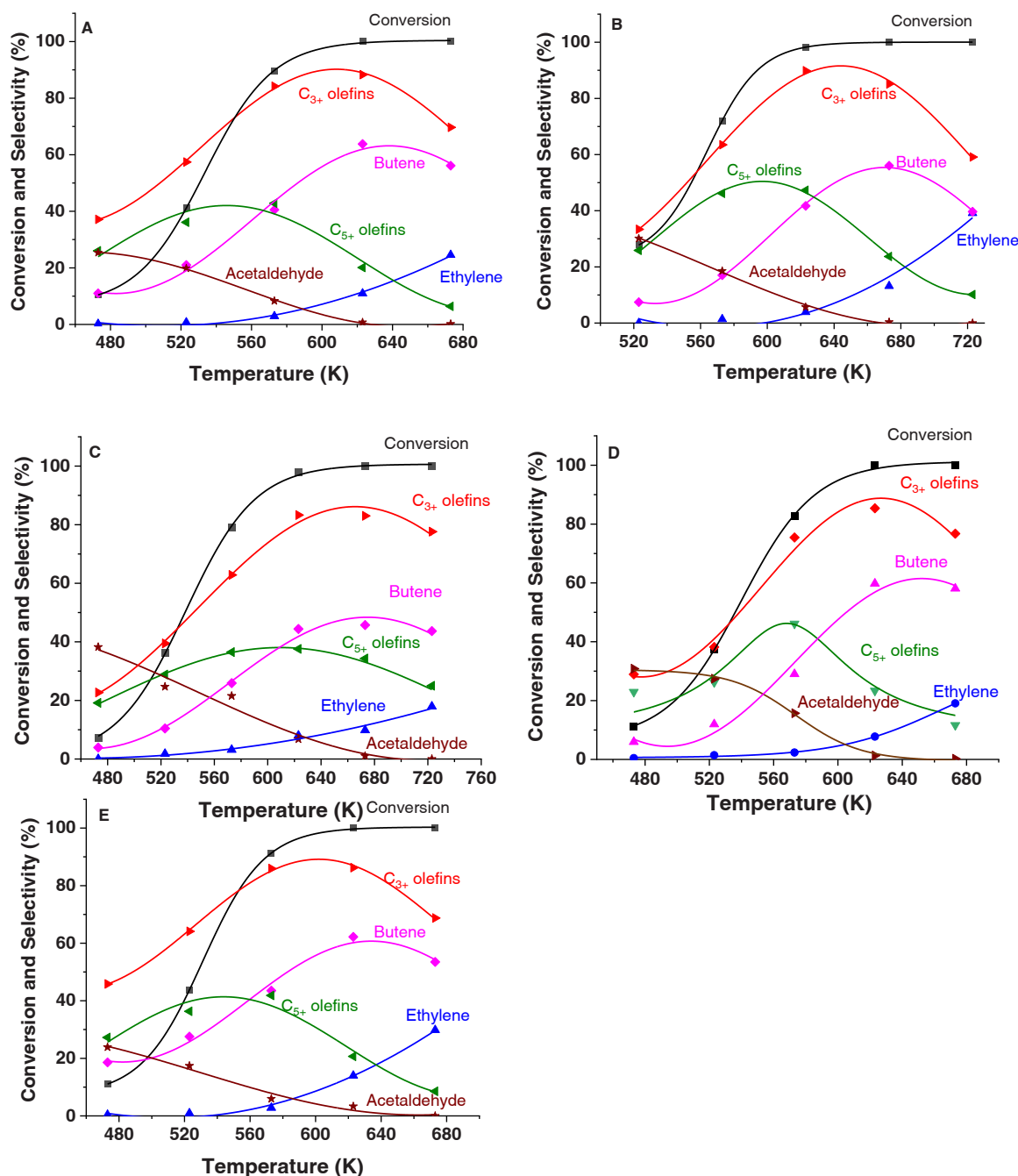

Fig. 9. The relative ratio of butene to C$_{5+}$ olefin in product stream as a function of the ionic radius of rare earth metal sites, simultaneously in line with the fraction of the initial rate of butanol dehydration to C-C coupling over bimetallic Cu-RE/Beta.

Fig. 10. Ethanol conversion and product selectivity over different Cu-RE/Beta catalysts as a function of reaction temperature: A) Cu-Y$_7$/beta, B) Cu−La$_{12}$/Beta, C) Cu-Ce$_{10}$/Beta D) Cu-Gd$_{12}$/Beta, E) Cu-Yb$_{12}$/Beta. (~0.20 g Cu-RE/Beta catalyst diluted in 0.8 g SiC, 0.53 h^{-1} WHSV, 7.5 kPa ethanol, 99.3 kPa H$_2$). Data is collected after 1.1 h time on stream (TOS).

consumed at higher reaction temperatures (573 K for Yb-, Y- and Gd-containing catalyst and 623 K for La and Ce-containing catalysts) due either to rapid aldol condensation of C$_4$ aldehyde intermediates (the precursor to butanol) or to increased dehydration to butene, ultimately reflecting the competing rates for aldol condensation or dehydration. This is supported by the optimized olefin product for C$_{5+}$ olefin at ~573 K or butene at or above 623 K. The TPRS results validate that the relative ratio of butene to C$_{5+}$ olefins in the product stream importantly depends on the competitive reactions between C-C coupling and C$_4$ alcohol dehydration, which can be adjusted by both the RE metal identity and the chosen reaction temperature.

4. Conclusion

In conclusion, we have developed bimetallic Cu-RE/Beta catalysts for the high selective production of C$_{3+}$ alkenes from ethanol conversion, specifically illustrating the role of the rare earth (RE) metal sites on alkene product distributions. The ratio of butene to C$_{5+}$ alkene products decreases over the Cu-RE/Beta catalysts as follows: Cu-Yb/Beta > Cu-Y/beta > Cu-Gd/Beta > Cu-Ce/Beta > Cu-La/Beta; this relationship is linearly correlated with the strength of Lewis acid RE sites. The relative rates of the competitive C-C coupling and C$_4$ alcohol dehydration reactions is the key factor for tailoring the alkene product distributions, which significantly rely on the nature of RE sites and the reaction temperature. Butene formation becomes dominant in a kinetic regime

where C_4 alcohol dehydration prevails, the formation of butene becomes dominant reaction pathway, which is the case for Cu-Yb$_{12}$/Beta, Cu-Y$_7$/beta and Cu-Gd$_{12}$/Beta catalysts with relative stronger Lewis acidity, yet the selectivity towards C_{5+} olefin formation in a kinetic regime favoring C-C bond formation. Such kinetic regimes are dependent not just on reaction temperature but on the selected RE metal identity and the associated Lewis acid strength of the RE active sites. C_{5+} olefins dominated the alkene distribution at relative low temperatures (below 573–623 K) and over RE-containing catalysts with weaker Lewis acid sites such as Cu-La$_{12}$/Beta. In contrast, higher temperatures and catalysts with stronger Lewis acid sites such as those on Cu-Yb$_{12}$/Beta favor increased butene formation. Taken together, these findings validate the capacity to tailor ethanol-to-olefin yields by varying the competing aldol condensation and dehydration reaction rates, which can be controlled by both the RE metal center identity and the reaction temperatures, allowing for the generation of a range of alkene products as intermediates for producing renewable fuels or chemicals.

CRediT authorship contribution statement

Kropf A. Jeremy: Formal analysis. **Hall Jacklyn:** Formal analysis. **Davison Brian:** Conceptualization, Funding acquisition. **Li Meijun:** Conceptualization, Data curation, Formal analysis, Investigation, Validation, Writing – original draft, Writing – review & editing. **Krause Theodore R.:** Formal analysis. **Sutton Andrew D.:** Funding acquisition, Investigation, Writing – review & editing. **Purdy Stephen C.:** Data curation, Writing – review & editing. **Li Zhenglong:** Conceptualization, Writing – review & editing. **Zhang Junyan:** Conceptualization, Writing – review & editing. **Unocic Kinga A.:** Formal analysis. **Lin Fan:** Data curation. **Wu Zili:** Resources, Writing – review & editing. **Cordon Michael:** Writing – review & editing. **Wang Huamin:** Writing – review & editing.

Declaration of Competing Interest

This manuscript has been authored in part by UT-Battelle, LLC, under contract DE-AC05–00OR22725 with the US Department of Energy (DOE). The US government retains and the publisher, by accepting the article for publication, acknowledges that the US government retains a nonexclusive, paid-up, irrevocable, worldwide license to publish or reproduce the published form of this manuscript, or allow others to do so, for US government purposes. DOE will provide public access to these results of federally sponsored research in accordance with the DOE Public Access Plan (http://energy.gov/downloads/doe-public-access-plan).

Data Availability

Data will be made available on request.

Acknowledgments

Appendix A. Supporting information

Supplementary data associated with this article can be found in the online version at doi:10.1016/j.apcatb.2023.123648.

References

[1] R.F. Association., 2019 Ethanol Industry Outlook, 2019.

[2] M. Balat, H. Balat, Recent trends in global production and utilization of bio-ethanol fuel, Appl. Energy 86 (2009) 2273–2282.

[3] US energy inforamtion adimiistration, short-term energy outlook, EIA.gov, 2023.

[4] J. Sun, Y. Wang, Recent advances in catalytic conversion of ethanol to chemicals, ACS Catal. 4 (2014) 1078–1090.

[5] L.R. Lynd, G.T. Beckham, A.M. Guss, L.N. Jayakody, E.M. Karp, C. Maranas, R. L. McCormick, D. Amador-Noguez, Y.J. Bomble, B.H. Davison, C. Foster, M. E. Himmel, E.K. Holwerda, M.S. Laser, C.Y. Ng, D.G. Olson, Y. Román-Leshkov, C. T. Trinh, G.A. Tuskan, V. Upadhayay, D.R. Vardon, L. Wang, C.E. Wyman, Toward low-cost biological and hybrid biological/catalytic conversion of cellulosic biomass to fuels, Energy Environ. Sci. 15 (2022) 938–990.

[6] S.P. Adhikari, J. Zhang, Q. Guo, K.A. Unocic, L. Tao, Z. Li, A hybrid pathway to biojet fuel via 2, 3-butanediol, Sustain. Energy Fuels 4 (2020) 3904.

[7] N.M. Eagan, M.D. Kumbhalkar, J.S. Buchanan, J.A. Dumesic, G.W. Huber, Chemistries and processes for the conversion of ethanol into middle-distillate fuels, Nat. Rev. Chem. 3 (2019) 223.

[8] B.G. Harvey, H.A. Meylemans, 1-hexene: a renewable C6 platform for full-performance jet and diesel fuels, Green. Chem. 16 (2014) 770.

[9] B.G. Harvey, R.L. Quintana, Synthesis of renewable jet and diesel fuels from 2-ethyl-1-hexene, Energy Environ. Sci. 3 (2010) 352.

[10] J.Q. Bond, D.M. Alonso, D. Wang, R.M. West, J.A. Dumesic, Integrated catalytic conversion of gamma-valerolactone to liquid alkenes for transportation fuels, Science 327 (80) (2010) 1110.

[11] R.A.L. Baylon, J. Sun, K.J. Martin, P. Venkitasubramanian, Y. Wang, Beyond ketonization: selective conversion of carboxylic acids to olefins over balanced Lewis acid–base pairs, Chem. Commun. 52 (2016) 4975–4978.

[12] R.D. Andrei, M.I. Popa, F. Fajula, V. Hulea, Heterogeneous oligomerization of ethylene over highly active and stable Ni-AlSBA-15 mesoporous catalysts, J. Catal. 323 (2015) 76–84.

[13] J. Saavedra Lopez, R.A. Dagle, V.L. Dagle, C. Smith, K.O. Albrecht, Oligomerization of ethanol-derived propene and isobutene mixtures to transportation fuels: catalyst and process considerations, Catal. Sci. Technol. 9 (2019) 1117–1131.

[14] A. Galadima, O. Muraza, Zeolite catalysts in upgrading of bioethanol to fuels range hydrocarbons: a review, J. Ind. Eng. Chem. 31 (2015) 1–14.

[15] V. Blay, E. Epelde, R. Miravalles, L.A. Perea, Converting olefins to propene: ethene to propene and olefin cracking, Catal. Rev. 60 (2018) 278–335.

[16] M.J. Cordon, J. Zhang, N.R. Samad, J.W. Harris, K.A. Unocic, M. Li, D. Liu, Z. Li, Ethanol conversion to C4+ olefins over bimetallic copper- and lanthanum-containing beta zeolite catalysts, ACS Sustain. Chem. Eng. 10 (2022) 5702–5707.

[17] V.L. Dagle, G. Collinge, M. Rahman, A. Winkelman, W. Hu, J.Z. Hu, L. Kovarik, M. Engelhard, J. Jocz, Y. Wang, M.-S. Lee, V.-A. Glezakou, D. Ray, R. Rousseau, R. Dagle, Single-step conversion of ethanol into n-butene-rich olefins over metal catalysts supported on ZrO2-SiO2 mixed oxides, Appl. Catal. B: Environ. 331 (2023), 122707.

[18] V.L. Dagle, A.D. Winkelman, N.R. Jaegers, J. Saavedra-Lopez, J. Hu, M. H. Engelhard, S.E. Habas, S.A. Akhade, L. Kovarik, V.-A. Glezakou, R. Rousseau, Y. Wang, R.A. Dagle, Single-step conversion of ethanol to n-butene over Ag-ZrO2/SiO2 catalysts, ACS Catal. 10 (2020) 10602–10613.

[19] J. Zhang, E.C. Wegener, N.R. Samad, J.W. Harris, K.A. Unocic, L.F. Allard, S. Purdy, S. Adhikari, M.J. Cordon, J.T. Miller, T.R. Krause, S. Cheng, D. Liu, M. Li, X. Jiang, Z. Wu, Z. Li, Isolated metal sites in Cu–Zn–Y/Beta for direct and selective butene-rich C3+ olefin formation from ethanol, ACS Catal. 11 (2021) 9885–9897.

[20] V.L. Sushkevich, I.I. Ivanova, Ag-promoted ZrBEA zeolites obtained by post-synthetic modification for conversion of ethanol to butadiene, ChemSusChem 9 (2016) 2216.

[21] W. Dai, S. Zhang, Z. Yu, T. Yan, G. Wu, N. Guan, L. Li, Zeolite structural confinement effects enhance one-pot catalytic conversion of ethanol to butadiene, ACS Catal. 7 (2017) 3703–3706.

[22] K. Mamedov, R.J. Davis, Cascade reaction of ethanol to butadiene over ag-promoted, silica- or zeolite-supported Ta, Y, Pr, or La oxide catalysts, ACS Catal. 13 (2023) 3333–3344.

[23] V.L. Sushkevich, D. Palagin, I.I. Ivanova, With open arms: open sites of ZrBEA zeolite facilitate selective synthesis of butadiene from ethanol, ACS Catal. 5 (2015) 4833–4836.

[24] P.I. Kyriienko, O.V. Larina, S.O. Soloviev, S.M. Orlyk, S. Dzwigaj, High selectivity of TaSiBEA zeolite catalysts in 1,3-butadiene production from ethanol and acetaldehyde mixture, Catal. Commun. 77 (2016) 123–126.

[25] C. Wang, M. Zheng, X. Li, X. Li, T. Zhang, Catalytic conversion of ethanol into butadiene over high performance LiZnHf-MFI zeolite nanosheets, Green. Chem. 21 (2019) 1006–1010.

[26] L. Qi, Y. Zhang, M.A. Conrad, C.K. Russell, J. Miller, A.T. Bell, Ethanol Conversion to Butadiene over Isolated Zinc and Yttrium Sites Grafted onto Dealuminated Beta, Zeolite, J. Am. Chem. Soc. 142 (2020) 14674.

[27] E.A. Cochran, K.N. Woods, D.W. Johnson, C.J. Page, S.W. Boettcher, Unique chemistries of metal-nitrate precursors to form metal-oxide thin films from solution: materials for electronic and energy applications, J. Mater. Chem. A 7 (2019) 24124–24149.

[28] H. Tsuruta, K. Yamaguchi, T. Imamoto, Tandem mass spectrometric analysis of rare earth(III) complexes: evaluation of the relative strength of their Lewis acidity, Tetrahedron 59 (2003) 10419–10437.

[29] O. Levenspiel, Experimental search for a simple rate equation to describe deactivating porous catalyst particles, J. Catal. 25 (1972) 265.

[30] S. Herrmann, E. Iglesia, Elementary steps in acetone condensation reactions catalyzed by aluminosilicates with diverse void structures, J. Catal. 346 (2017) 134–153.

[31] R. Shannon, Revised effective ionic radii and systematic studies of interatomic distances in halides and chalcogenides, Acta Crystallogr. Sect. A 32 (1976) 751–767.

[32] X. Wang, M. Li, Z. Wu, In situ spectroscopic insights into the redox and acid-base properties of ceria catalysts, Chin. J. Catal. 42 (2021) 2122–2140.

[33] G. Turnes Palomino, J. José Cuart Pascual, M. Rodríguez Delgado, J. Bernardo Parra, C. Otero Areán, FT-IR studies on the acidity of gallium-substituted mesoporous MCM-41 silica, Mater. Chem. Phys. 85 (2004) 145.

[34] K. Chalupka, R. Sadek, L. Valentin, Y. Millot, C. Calers, M. Nowosielska, J. Rynkowski, S. Dzwigaj, Dealuminated beta zeolite modified by alkaline earth, Met., J. Chem. 2018 (2018) 1–11.

[35] G. Connell, J. Dumesic, The generation of Brønsted and Lewis acid sites on the surface of silica by addition of dopant cations, J. Catal. 105 (1987) 285.

[36] G. Xiong, H. Yang, L. Liu, J. Liu, Post-synthesis of Sn-beta zeolite by aerosol method, RSC Adv. 13 (2023) 4835–4842.

[37] C. Morterra, G. Cerrato, On the use of pyridine adsorption as an analytical tool in surface chemistry, Langmuir 6 (1990) 1810–1812.

[38] P. Boroń, L. Chmielarz, J. Gurgul, K. Łątka, B. Gil, J.-M. Krafft, S. Dzwigaj, The influence of the preparation procedures on the catalytic activity of Fe-BEA zeolites in SCR of NO with ammonia and N2O decomposition, Catal. Today 235 (2014) 210–225.

[39] A.M. Camiloti, S.L. Jahn, N.D. Velasco, L.F. Moura, D. Cardoso, Acidity of Beta zeolite determined by TPD of ammonia and ethylbenzene disproportionation, Appl. Catal. A: Gen. 182 (1999) 107–113.

[40] H. Zhang, M.Y.S. Ibrahim, D.W. Flaherty, Aldol condensation among acetaldehyde and ethanol reactants on TiO2: Experimental evidence for the kinetically relevant nucleophilic attack of enolates, J. Catal. 361 (2018) 290–302.